ROYAL SOCIETY
OF CHEMISTRY

EDGE ARTICLE

Check for updates

All publication charges for this article
have been paid for by the Royal Society
of Chemistry

Probing the stability of metal–organic frameworks by structure-responsive mass spectrometry imaging†

Yue Lin,[ab] Ke Min,[a] Wende Ma,[a] Xuezhi Yang,[b] Dawei Lu,[a] Zhenyu Lin, [c]
Qian Liu [*ade] and Guibin Jiang[ae]

The widespread application of metal–organic frameworks (MOFs) is seriously hindered by their structural instability and it is still very challenging to probe the stability of MOFs during application by current techniques. Here, we report a novel structure-responsive mass spectrometry (SRMS) imaging technique to probe the stability of MOFs. We discovered that intact CuBTC (as a model of MOFs) could generate the characteristic peaks of organic ligands and carbon cluster anions in laser desorption/ionization mass spectrometry, but these peaks were significantly changed when the structure of CuBTC was dissociated, thus enabling a label-free probing of the stability. Furthermore, SRMS can be performed in imaging mode to visualize the degradation kinetics and reveal the spatial heterogeneity of the stability of CuBTC. This technique was successfully applied in different application scenarios (in water, moist air, and CO_2) and also validated with different MOFs. It thus provides a versatile new tool for better design and application of environment-sensitive materials.

Introduction

Metal–organic frameworks (MOFs) are formed with metal ions as coordination centers and organic linkers and have been proposed as alternatives and even better materials over traditional materials in various fields including catalysts, gas absorption, separation, and biomedicine.[1–9] Some exceptional properties such as high porosity, ultralarge surface areas, and chemically tunable structures of MOFs make them easy and efficient for gas storage and capture.[10–12] However, many gases such as water vapor, NO_x, NH_3, H_2S, and SO_x are very likely to destroy the structures of MOFs by binding with metal clusters when the metal centers are not sufficiently inert.[13–16] Especially for water vapor, quantum mechanical calculations based on cluster models have predicted that water molecules could insert into the metal–ligand bonds to induce ligand displacement and hydrolysis.[17] Thus, the performance of MOFs usually deteriorates during a long-term use because water vapor is ubiquitous in industrial flue gas (∼10%) and ambient air.[18] Although many strategies have been developed to improve the stability of MOFs,[19,20] techniques for probing the performance and structural intactness of MOFs in complex media are still lacking.

Current techniques for MOF characterization are mainly based on electron microscopy,[19,21,22] X-ray diffraction (XRD),[23,24] and Fourier transform infrared spectroscopy (FTIR).[25,26] However, these techniques are less tolerable to complex media and give insufficient chemical information for structural identification. The technical bottlenecks seriously limit the monitoring of MOFs' stability during their applications, and new methods are imperative for probing the degradation of MOFs to ensure the application efficiency. In this regard, mass spectrometry (MS) emerges as a tool to fill such a technical gap. Compared with other characterization techniques, MS can provide multi-dimensional information including precise molecular weight and plenty of molecular structural information,[27] enabling its use as a powerful tool for characterization of nanomaterials.[28–31] Moreover, in the last decade, the development of MS imaging technology has greatly improved the *in situ* analytical capability of spatial resolution.[32] It is noteworthy that MS is capable of simultaneously analyzing organic and inorganic species, which well meets the characterization demand of metal ions and organic linkers in MOFs.

Herein, we report a novel structure-responsive mass spectrometry (SRMS) technique for characterization and stability monitoring of MOFs under different conditions (Fig. 1A).

aState Key Laboratory of Environmental Chemistry and Ecotoxicology, Research Center for Eco-Environmental Sciences, Chinese Academy of Sciences, Beijing 100085, China. E-mail: qianliu@rcees.ac.cn

*bSchool of Environment, Hangzhou Institute for Advanced Study, UCAS, Hangzhou 310024, China*

cMinistry of Education Key Laboratory for Analytical Science of Food Safety and Biology, Fujian Provincial Key Laboratory of Analysis and Detection for Food Safety, College of Chemistry, Fuzhou University, Fuzhou, Fujian, 350116, China

dInstitute of Environment and Health, Jianghan University, Wuhan 430056, China

eUniversity of Chinese Academy of Sciences, Beijing 100190, China

† Electronic supplementary information (ESI) available. See DOI: https://doi.org/10.1039/d4sc00021h
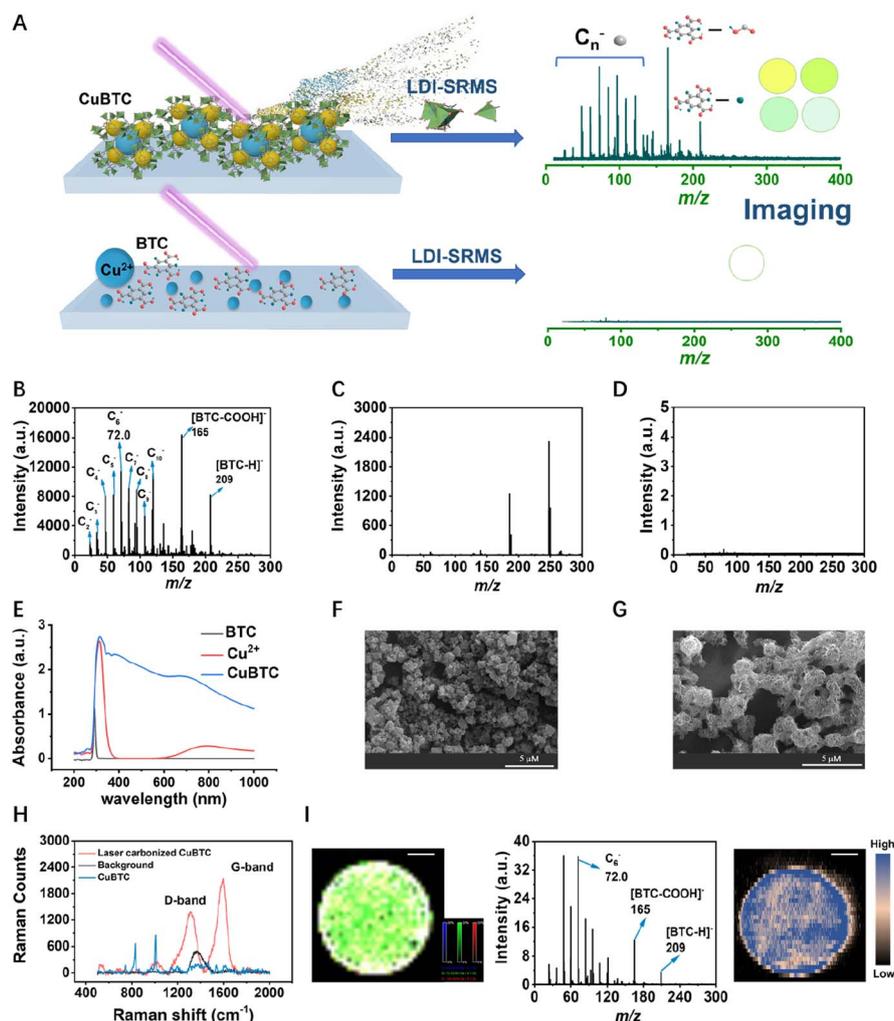
Fig. 1 LDI-SRMS and multi-chemical characterization of CuBTC. (A) Schematic diagram of the LDI-SRMS imaging technique for CuBTC characterization. LDI-SRMS results of (B) CuBTC (1 mg mL^{-1}), (C) BTC (1 mg mL^{-1}) and (D) Cu(NO$_3$)$_2$ (1 mg mL^{-1}). (E) UV-vis spectra of CuBTC, Cu(NO$_3$)$_2$ and BTC. SEM images of (F) CuBTC and (G) laser carbonized CuBTC. (H) Raman spectroscopy of CuBTC and laser carbonized CuBTC (the background spectrum is from the ITO glass). (I) Characterization of CuBTC at 1 mg mL^{-1}. The left column shows the LDI-SRMS imaging result and the original image color of each ion is generated by the primary colors red (m/z 165), green (m/z 72.0) and blue (m/z 209). The middle column shows the corresponding LDI-SRMS result, and the right column shows the laser ablation inductively coupled plasma mass spectrometer (LA-ICP-MS) imaging result. The spatial resolution of MS imaging is 50 μm and the scale bar is 500 μm.

CuBTC (BTC = benzene-1,3,5-tricarboxylic acid) was chosen as a model MOF that was formed with Cu as the coordination center and BTC as the organic linker. It is one of the most frequently studied MOFs as well as the first commercially available MOF, but its practical application was hindered primarily due to the limited stability of the MOF towards moisture.[33–36] We found that strong laser desorption/ionization mass spectrometry (LDI-MS) signals from BTC are only present in nanostructured CuBTC but absent in pure BTC solution. Thus, if the structure of CuBTC decays (*e.g.*, upon hydrolysis), the LDI-MS signals and imaging results would change sensitively and synchronously. Meanwhile, the signal of Cu in CuBTC can be simultaneously monitored by laser ablation inductively coupled plasma mass spectrometry (LA-ICP-MS) imaging, which is not structure-responsive and thus can be used as a control for

CuBTC. In this way, SRMS provides a versatile tool for characterization, quantification, and stability probing of MOFs.

Results and discussion

LDI-SRMS and multi-chemical characterization of CuBTC

To demonstrate this concept, we first tested the specific fragment peaks of CuBTC, BTC, and Cu^{2+} generated in LDI-SRMS. Fig. 1B shows that several characteristic fragment ions consisting of carbon cluster anions (C$_2^-$–C$_{10}^-$), [BTC-COOH]$^-$ (m/z 165) and [BTC-H]$^-$ (m/z 209) of CuBTC were observed in LDI-SRMS, but these were absent for pure BTC (Fig. 1C). When we mixed the BTC standard with α-cyano-4-hydroxycinnamic acid (CHCA) as an ionization-assisted matrix, two characteristic peaks at m/z 165 and 209 in LDI-TOF MS were also obtained. According to the secondary MS information, the fragment ions

from the two characteristic precursor ions for CuBTC and BTC + CHCA were consistent (Fig. S1†), indicating that the characteristic peak signals of CuBTC were produced from BTC. In addition, $Cu(NO_3)_2$ did not produce any MS signal (Fig. 1D). The specific response of LDI-SRMS to CuBTC can be attributed to its unique physico-chemical properties. CuBTC exhibited strong light absorption ability in 350–400 nm (Fig. 1E and S2†), which well matches the wavelength (355 nm) of the laser used in LDI-MS and could greatly facilitate efficient laser energy absorption and transfer to target molecules for ionization. It is noteworthy that the MS peaks of carbon clusters ($[C_n]^-$) were usually specifically generated by inorganic carbon materials, such as graphene, black carbon, and carbon nanotubes.[32,37] To the best of our knowledge, this is also the first report that MOFs can also generate $[C_n]^-$ peaks in LDI-MS. According to the SEM results, the morphologies of MOFs changed from an irregular blocky structure to a network structure under the laser (Fig. 1F and G). Raman results showed that the network material presented the G-peak signal at ~1600 cm^{-1} and the D-peak signal at ~1330 cm^{-1} belonging to the specific signals of carbon materials (Fig. 1H). So, the generation of $[C_n]^-$ peaks of CuBTC can be attributed to the rapid transformation of MOFs into carbon structures by laser-induced carbonization.[38–40] Overall, the characteristic peaks of BTC (m/z 165 and 209) and $[C_n]^-$ were only present in CuBTC MOFs but absent in pure BTC.

Furthermore, SRMS can be performed in imaging mode to spatially probe the stability of CuBTC. The traditional point-to-point sampling model in LDI-MS usually suffers from poor reproducibility, especially considering the heterogeneous distribution of nanostructures on the target. Thus, MS imaging covering a certain spatial region could probe the MOFs with higher accuracy and reproducibility. We chose three characteristics peaks (m/z 72.0, 165, and 209) for LDI-SRMS imaging of CuBTC and the content of Cu was also detected by LA-ICP-MS as a control. As shown in Fig. 1I and S3,† the color intensity of the MS images faded in both LDI-SRMS and LA-ICP-MS imaging. The characteristic fragment (m/z at 165) generated by the loss of a carboxyl group of BTC in negative-ion mode was used as a marker for quantification of CuBTC (Fig. S4†).

The phenomenon that the MS signals of CuBTC are dependent on the formation of its unique spatial structure inspired us to monitor the stability of CuBTC by SRMS. CuBTC is capable of absorbing laser energy and transferring it to its organic ligands, facilitating ionization and generating signals at m/z 165. Upon the collapse of the CuBTC structure, there is a concurrent decrease in its capacity to absorb laser energy and promote ionization, leading to a reduced peak intensity at m/z 165. This structural collapse also results in a diminished $[C_n]^-$ peak. However, the m/z 165 peak, which relies on the MOF structure for energy absorption and subsequent ligand ionization, is more significantly impacted by the structural disintegration. To verify our hypothesis, we compared the LDI-SRMS results of newly synthesized CuBTC (CuBTC-1) and aged CuBTC (CuBTC-2, aged for two months after synthesis) (Fig. S5A and B†). The two materials showed similar LDI-SRMS patterns, but the peaks ratio of m/z 165 to m/z 72.0 ($I_{m/z\ 165}/I_{m/z\ 72.0}$) of CuBTC-1 was higher than that of CuBTC-2, indicating that the structure of

aged CuBTC has slightly changed compared with that of fresh CuBTC. In many application scenarios, water vapor was suspected to be the main factor to affect the performance and stability of CuBTC, since it is ubiquitous in air and various industrial emissions.[41,42] Previous studies have showed that under long-time exposure with high water content, the crystal lattice, porosity, and surface area of MOFs could be changed or completely destroyed.[42,43] Thus, to explore the stability of MOFs (i.e., CuBTC) in the aquatic environment, we also dispersed CuBTC-1 in distilled water instead of ethyl alcohol. The results showed that CuBTC-1 in distilled water had a remarkably lower peak intensity at m/z 165 than m/z 72.0 (Fig. S5C†), indicating that water could greatly induce the degradation of CuBTC and that the change of the intensity ratio of characteristic peaks in LDI-SRMS ($I_{m/z\ 165}/I_{m/z\ 72.0}$) provides a sensitive indicator for stability probing of CuBTC.

Probing the stability of CuBTC in water

Next, when CuBTC-1 was dispersed in water for 4 h, the appearance changed greatly during the degradation process. As shown in Fig. 2A and B, the color of CuBTC changed from blue to light blue, indicating some complex or copper hydroxide formation, and the morphology changed from nanoaggregates into micro-belts.[44,45] $I_{m/z\ 165}/I_{m/z\ 72.0}$ was further applied to describe the water stability of CuBTC. As shown in Fig. 2C, the ratio dropped rapidly in 120 min and tended to be steady in 120–240 min and the $I_{m/z\ 165}/I_{m/z\ 72.0}$ ratio stabilized below 0.2, indicating that CuBTC would be completely degraded within 120 min in the aquatic environment. Previous research has shown the strong affinity of water molecules to Cu centers in the CuBTC framework.[46,47] So, as a result of the attack of water molecules on the Cu centers and the substitution ligands, BTC peaks gradually disappeared during the degradation process. The degradation followed a kinetic process ($y = 0.742e^{-x/34.5} + 0.188, R^2 = 0.9806$). To investigate the significant decrease in the characteristic signals of degraded CuBTC observed in LDI-MS, we tested the light absorption capacity of CuBTC both before and after degradation. The UV absorption of degraded CuBTC at 350–400 nm is much lower than that of non-degraded CuBTC at the same concentration (Fig. 2D), indicating a diminished efficiency in laser absorption and more difficulty for ionization.

To explore the spatial difference of CuBTC stability, we performed SRMS imaging to monitor the stability of CuBTC in the aquatic environment with a spatial resolution of 50 μm (Fig. 2E). The characteristic fragment ions of CuBTC consisting of C_6^- (m/z 72.0, in green), $[BTC-COOH]^-$ (m/z 165, in red) and $[BTC-H]^-$ (m/z 209, in blue) were chosen for MS imaging and the results are shown in Fig. 2F–I and S6.† CuBTC exhibited a tendency to aggregate at the periphery of the droplet, a phenomenon known as the coffee-ring effect. Consequently, the imaging intensity of m/z 165 and 209 from the outer layer of the dried droplet was higher than those at the center. This can be attributed to the more rapid evaporation rate of water in the MOFs at the edge during the drip drying process, compared to those at the center, resulting in a lower degree of degradation induced by water exposure. Additionally, the imaging intensity of m/z 165 and 209 further decreased, indicating that the CuBTC was degraded
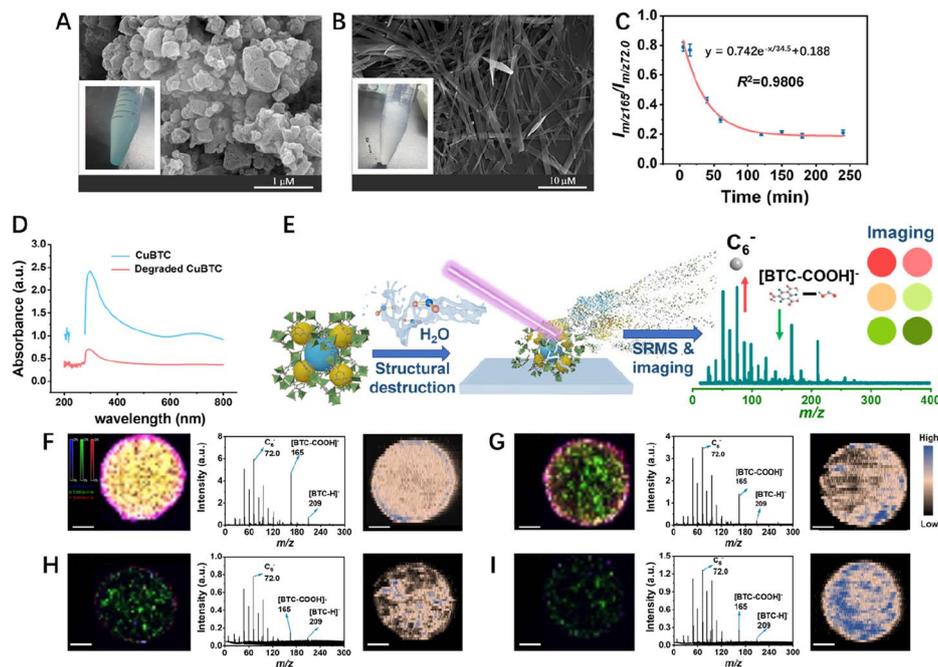
Fig. 2 Characterization of CuBTC in water. SEM and optical images of CuBTC in water for (A) 5 min and (B) 240 min. (C) The relationship between the intensity ratio of m/z 165 and 72.0 ($I_{m/z\ 165}/I_{m/z\ 72.0}$) and the standing time in water. (D) UV-vis spectra of CuBTC and degraded CuBTC (CuBTC underwent degradation by exposing to water for 120 minutes). (E) Schematic diagram of the degradation process for CuBTC. MS characterization of CuBTC in water for different periods of time. Standing time: (F) 5 min, (G) 40 min, (H) 120 min and (I) 180 min. For each standing time, the left column shows the LDI-SRMS imaging result and the original image color of each ion is generated by the primary colors red (m/z 165), green (m/z 72.0) and blue (m/z 209). The middle column shows the corresponding LDI-SRMS result, and the right column shows the LA-ICP-MS imaging result. The spatial resolution of imaging is 50 μm and the scale bar is 500 μm. The slight difference in Cu^{2+} concentration was irregular and might come from the slightly different mass of CuBTC in each drop sample, because MOFs are difficult to disperse and drop uniformly.

gradually as the exposure time prolonged (Fig. 2F–I and S6,† the left and middle columns). In addition, the concentration of Cu^{2+} was independent of the structure of CuBTC, and thus it was monitored by LA-ICP-MS for control to assess the difference of the initial amount of CuBTC in different samples. The results showed that the distribution of Cu^{2+} obtained by LA-ICP-MS imaging overlapped with that of CuBTC obtained by LDI-SRMS imaging, but the signal intensity of Cu^{2+} showed no time-dependence, indicating that the initial amount of the added CuBTC for different exposure times was consistent (Fig. 2F–I and S6,† the right column). Moreover, the consistent concentration of the Cu^{2+} center throughout the process indicated that the metal center's influence on LDI-MS should remain constant, thereby not affecting our characterization outcomes. During this process, the morphology of CuBTC changed significantly as the exposure time was prolonged and finally transformed into micro-size particles (Fig. S7†). The XRD and FTIR spectra and N$_2$ absorption results showed that the crystallographic plane, chemical structure, Brunauer–Emmett–Teller (BET) surface area, pore volume and pore size also changed (Fig. S8–S10 and Table S2, see the ESI† for detailed discussion), which may be the reason for the decrease of soft desorption/ionization efficiency in MS. Overall, the SRMS imaging can reflect the spatial difference of the stability of MOFs.

Spatial heterogeneity of the stability of CuBTC in complex air medium

Besides water, other substances in air may also contribute to the degradation of CuBTC. We placed CuBTC in moist air with a relative humidity (RH) of 80% to monitor the stability of CuBTC (dispersed in ethanol to avoid the influence of aqueous solvents). During the degradation process of CuBTC, the complex species in the air may attack the metal centers resulting the slow dissociation of the CuBTC nanostructure. So, the $I_{m/z\ 165}/I_{m/z\ 72.0}$ ratio decreased as the exposure time increased and the BTC-associated peaks were lost (Fig. 3A). Finally, under the erosion of complex substances mainly due to water vapor in the air, the degradation degree of CuBTC tends to be stable within 720 h, and the $I_{m/z\ 165}/I_{m/z\ 72.0}$ ratio is stable below 0.15 (it is not excluded that new degradation phenomena may occur with the extension of time).

The MS imaging suggested the high production amounts of [BTC-COOH]$^-$ and [BTC-H]$^-$ in the beginning of exposure. Then, the overlayed image turned green with the exposure time prolonging, indicating the decrease of the MS signals of [BTC-COOH]$^-$ and [BTC-H]$^-$ (Fig. 3B–H, the left and middle columns). Meanwhile, LA-ICP-MS imaging was also used to monitor the Cu concentration along with the SRMS imaging for comparison and verified that the variation of SRMS imaging was derived from the degradation of CuBTC (see Fig. S12†). In
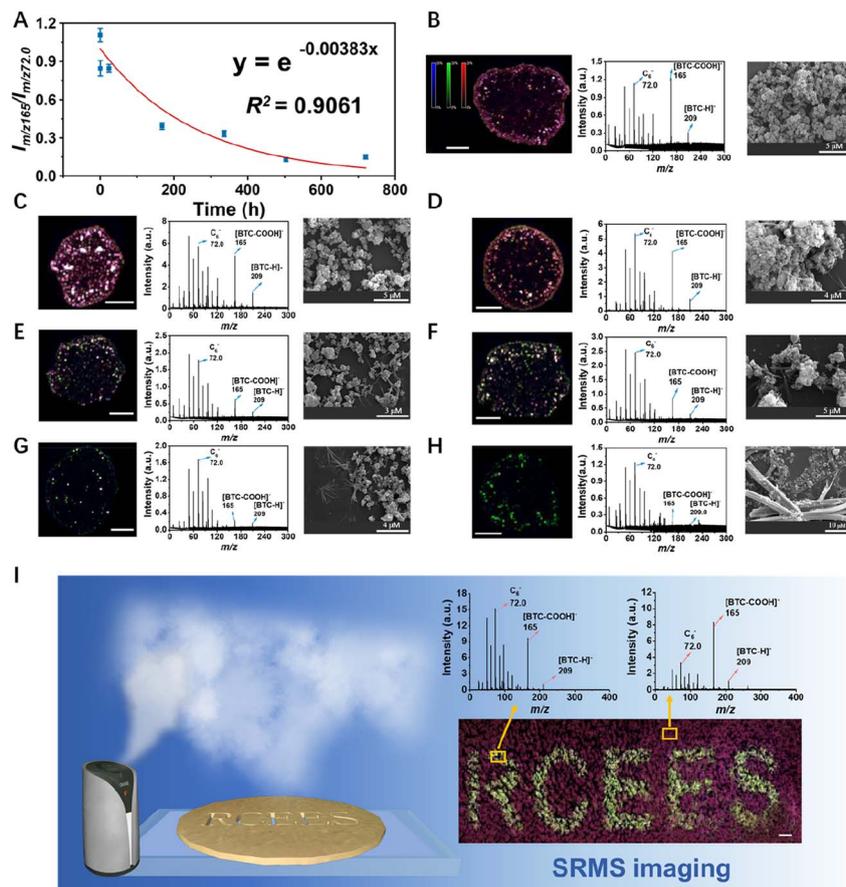
Fig. 3 Characterization of CuBTC after exposed to air for different periods of time. (A) The relationship between the intensity ratio of m/z 165 and 72.0 ($I_{m/z\ 165}/I_{m/z\ 72.0}$) and the exposure time in air. LDI-SRMS and SEM results of different exposure times: (B) 10 min, (C) 30 min, (D) 24 h, (E) 168 h, (F) 336 h, (G) 504 h, and (H) 720 h. For each exposure time, the left column shows the LDI-SRMS imaging result and the original image color of each ion is generated by the primary colors red (m/z 165), green (m/z 72.0) and blue (m/z 209). The middle column shows the corresponding LDI-SRMS result, and the right column shows the SEM pictures of CuBTC. (I) Characterization ability of spatial stability for CuBTC by the SRMS imaging technique. The spatial resolution of MS imaging is 50 μm and the scale bar is 1 mm.

addition, during the degradation process in the air, we also observed the morphological change and the production of degenerative CuBTC microparticles at an exposure time of up to 30 days (Fig. 3B–H, the right column, Fig. S13†).

It is worth mentioning that SRMS can probe the degradation of CuBTC with high sensitivity within 30 min in complex air medium (Fig. 3B and C). However, when using the traditional SEM technique, the morphology only presented a little difference with some micro-belts being observed until 24 h (Fig. 3C and D). In addition, thermogravimetric (TG) analysis was unable to provide any information changed within 240 min in the aquatic environment (Fig. S11†). XRD and FTIR results also showed no observable change of the crystal structure even within 150 min (Fig. S8 and S9†). Similarly, BET measurements displayed no observable change of N_2 uptake capacities, BET surface area, pore volume and pore size within 40 min (Fig. S10†). In contrast to these traditional methods, SRMS can give molecular information of the materials during the degradation process to enable the selective detection of MOFs in complex media. Moreover, the SRMS method only requires a very low quantity of sample (i.e., ~1 μg CuBTC), with which

XRD, FTIR or BET techniques are difficult to process. Therefore, the SRMS technique has shown advantages including higher sensitivity, lower sample dosage required, and stronger capability for CuBTC identification than traditional microscopic and spectroscopic techniques.

Besides, in various applications of MOFs, they are usually coated at the surface of substrates to form a MOF film to provide the desired functionality such as catalysis, gas separation, storage, or sensor applications.[48,49] When a MOF film encounter interfering molecules during the application process (either from the ambient environment or from the target), its stability may differ spatially. So, here we applied the SRMS imaging technique to characterize the spatial difference of CuBTC stability. As shown in Fig. 3I, CuBTC was coated on the surface of ITO glass and a patterned shield was put on the top of the ITO glass with a predesigned pattern (letters of "RCEES"). After 12 h exposure of moist air, the CuBTC coating was characterized by SRMS, and the pattern caused by the water-induced CuBTC degradation could be clearly visualized. This result showed that the SRMS imaging can sensitively and spatially visualize the stability of Cu-MOFs.

Spatial heterogeneity and degradation kinetics of the stability of MOFs in the process of CO_2 capture

To demonstrate the real applicability of this technique, we further used it to monitor the stability of MOFs during the CO_2 adsorption application. MOFs are excellent adsorbents for CO_2 capture from air because of their porous nature, large surface areas, and high affinity for gas molecules.[50] They show great potential in reducing carbon emission and curbing global warming. In the process of CO_2 capture, the stability and behavior of MOFs in humid environments are extremely important.[42,51] Many technical routes have been developed to improve the performance and stability of MOFs but challenges retain in characterization and monitoring of the structural intactness of MOFs during the process of CO_2 capture. In this regard, SRMS provides a feasible approach to address this challenge.

To this end, CuBTC was placed in a CO_2 airflow with a humidity of 80% RH for the subsequent test. Such a level of humidity is typical in humid climate or industrial exhaust scenarios. As shown in Fig. 4, CuBTC in CO_2 presented a characteristic peak at m/z 254 assigned to the absorption of CO_2 (M_w 44) to BTC (M_w 210), which was absent for CuBTC in air. In addition, the $I_{m/z\ 165}/I_{m/z\ 72.0}$ of the CO_2 (2.68) group was notably higher than the $I_{m/z\ 165}/I_{m/z\ 72.0}$ of air (1.16), indicating that CO_2 was very likely to be able to protect CuBTC from degradation to some extent. In the stability monitoring process of CuBTC in CO_2, the concentration ratio of $[BTC\text{-}COOH]^-$ and $[BTC\text{-}H]^-$ (m/z 165 and 209) was high at the beginning stage and then decreased (Fig. S14†). The $I_{m/z\ 165}/I_{m/z\ 72.0}$ ratio also decreased as the adsorption time increased, indicating the slow degradation of CuBTC in CO_2 (Fig. S15†). The degradation kinetics of CuBTC in CO_2 of high concentration was overall similar to that in moist air and the $I_{m/z\ 165}/I_{m/z\ 72.0}$ ratio was finally stable below 0.15.

Universality of SRMS imaging techniques

The proposed technique of SRMS imaging is achieved based on the variations in LDI-MS signals caused only by changes in the intactness of the structure (and its associated laser energy absorption capability). Based on this, SRMS can be applied to more types of MOFs. The universality of the proposed techniques was firstly demonstrated by using other types of Cu-MOFs that may be less stable (*i.e.*, Cu(QC)$_2$, SIFSIX-1-Cu, SIFSIX-2-Cu-i, SIFSIX-3-Cu, CPL-1, CPL-2, and CPL-5). After the Cu-MOFs were placed in water for different periods of time (5 min, 1.5 h, 3 days and 7 days), the relative intensities of the characteristic peaks for some Cu-MOFs changed accordingly, indicating that their stability and structure were deteriorated in water. Meanwhile, the corresponding SRMS imaging results also changed significantly (see Fig. 5, S16–S18 and Table S5†). Take Cu(QC)$_2$ as an example, the peaks at m/z 114, 127, 143, 169, 212, 220, 246 and 287 were chosen for the SRMS imaging because the changes of the relative MS intensities were mainly located between m/z 50 and m/z 300 (Fig. S14†). The peak at m/z 169 was chosen as a reference. The ratios of $I_{m/z\ 114}/I_{m/z\ 169}$, $I_{m/z\ 127}/I_{m/z\ 169}$, $I_{m/z\ 143}/I_{m/z\ 169}$ and $I_{m/z\ 212}/I_{m/z\ 169}$ showed increasing trends but the ratios of $I_{m/z\ 220}/I_{m/z\ 169}$, $I_{m/z\ 246}/I_{m/z\ 169}$ and $I_{m/z\ 287}/I_{m/z\ 169}$ declined as the exposure time in water was prolonged. Both the increasing or decreasing ratios of signal peak intensities could be used to characterize the degradation process of Cu(QC)$_2$. Similarly, the MS signals for the SIXSIF series (1,2-bis(4-pyridyl)ethyne as the ligand) exhibited changes as the exposure time in water increased (Table S5, Fig. S17 and S18†). In contrast, SEM results showed little morphological change during the first 3 days (Fig. S19A and B†). This result again demonstrated the sensitivity of the SRMS method. For the CPL series (2,3-pyrazinedicarboxylic acid as the ligand), the MS
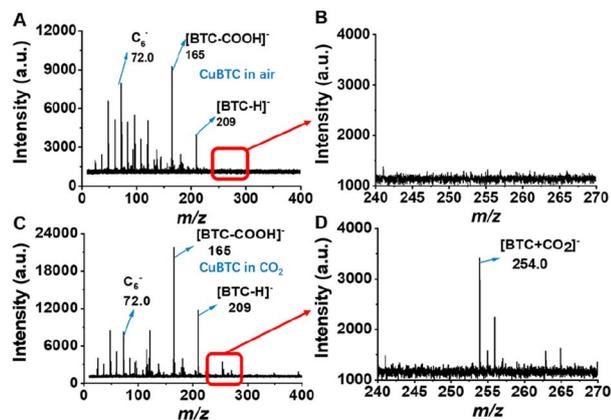

Fig. 4 LDI-SRMS of CuBTC in (A) air and (B) the corresponding enlarged drawing of (A), m/z 240–270, (C) CO_2 and (D) the corresponding enlarged drawing of (C), m/z 240–270.
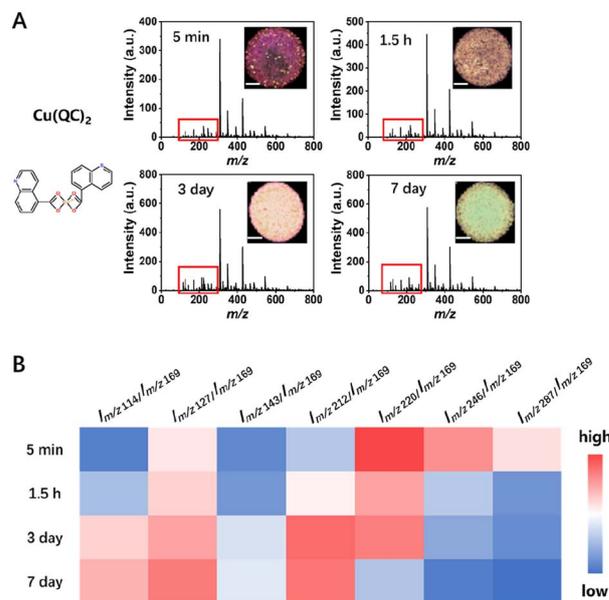

Fig. 5 Characterization of Cu(QC)$_2$ in water for different periods of time (standing time: 5 min, 1.5 h, 3 days and 7 days). (A) LDI-SRMS results of Cu(QC)$_2$. The main characteristic peaks of change are in the red box and Fig. S11† (inset shows the corresponding imaging results). The spatial resolution of imaging is 50 μm and the scale bar is 500 μm. (B) Heat map of the intensity ratio for the characteristic peaks of Cu(QC)$_2$.

signals remained relatively stable, and the SEM results also showed no significant changes (Fig. S19C–E†). Thus, the stability of different components and synthesis methods for MOFs could be reflected by the SRMS method.

Notably, several non-copper MOFs including MIL-101(Cr), Ni-containing MOFs, ZIF-8(Zn), and MOF-74(Zn) also presented SRMS signals in LDI-MS, indicating that the proposed technique can be extended to characterization and stability monitoring of more types of MOFs (Fig. S20†). Most of these materials had some UV absorption at 355 nm, which could explain why they were able to absorb laser energy and produced characteristic ions in LDI-SRMS (Fig. S21†). More detailed discussion is presented in the ESI.† Therefore, the proposed SRMS technique is applicable for different types of MOFs.

Conclusions

In summary, this work developed a novel and efficient SRMS imaging technique based on the discovery that MOFs could generate structure-specific signals in LDI-MS. With CuBTC as a MOFs model, the MS signals at m/z 72.0, 165 and 209 showed high dependence of the nanostructure of CuBTC in multiple media including water, air and CO_2, and the peak ratio of $I_{m/z\ 165}/I_{m/z\ 72.0}$ can be used as an indicator to accurately monitor the stability of CuBTC with high spatial resolution. In addition, the degradation kinetics and spatial heterogeneity of the stability of CuBTC were visualized further by SRMS imaging. It has great potential to characterize and monitor the synthetic process, stability and degradation mechanisms of MOFs with different metal centers. Compared with traditional characterization techniques, SRMS shows the advantages of high sensitivity, good precision, low sample consumption, rapidity, and capability of *in situ* analysis. At the same time, the SRMS method also has some limitations, *e.g.*, it is not able to directly reflect the morphological change of the material and needs expensive instrument, so it is better to use it together with traditional techniques such as SEM to obtain multi-dimensional information about the degradation process of materials. Overall, it provides an efficient tool for stability monitoring for MOFs or other nanomaterials in a variety of complex environments and application processes, thus opening a new avenue for better design and application of environment-sensitive new materials.

Data availability

All experimental procedures and ESI tables and figures are available in the ESI.†

Author contributions

Q. Liu conceived and designed the research; Y. Lin performed most of the experiments; K. Min, W. Ma, X. Yang, D. Lu and Z. Lin helped with the experiments; G. Jiang supervised the project; Y. Lin and Q. Liu analyzed the data; Y. Lin and Q. Liu wrote the paper.

Conflicts of interest

There are no conflicts to declare.

Acknowledgements

Notes and references

1 J. W. M. Osterrieth and D. Fairen-Jimenez, Metal–Organic Framework Composites for Theragnostics and Drug Delivery Applications, *Biotechnol. J.*, 2021, **16**, 2000005.

2 X. Yue, N. L. Ma, C. Sonne, R. Guan, S. S. Lam, Q. V. Le, X. Chen, Y. Yang, H. Gu, J. Rinklebe and W. Peng, Mitigation of indoor air pollution: a review of recent advances in adsorption materials and catalytic oxidation, *J. Hazard. Mater.*, 2021, **405**, 124138.

3 M. Eddaoudi, J. Kim, N. Rosi, D. Vodak, J. Wachter, M. O'Keeffe and O. M. Yaghi, Systematic design of pore size and functionality in isoreticular MOFs and their application in methane storage, *Science*, 2002, **295**, 469–472.

4 M. Xu, P. Cai, S.-S. Meng, Y. Yang, D.-S. Zheng, Q.-H. Zhang, L. Gu, H.-C. Zhou and Z.-Y. Gu, Linker Scissoring Strategy Enables Precise Shaping of Metal–Organic Frameworks for Chromatographic Separation, *Angew. Chem., Int. Ed.*, 2022, **61**, e202207786.

5 P. Horcajada, R. Gref, T. Baati, P. K. Allan, G. Maurin, P. Couvreur, G. Ferey, R. E. Morris and C. Serre, Metal–Organic Frameworks in Biomedicine, *Chem. Rev.*, 2012, **112**, 1232–1268.

6 J. Qiu, F. Wang, T. Zhang, L. Chen, Y. Liu, F. Zhu and G. Ouyang, Novel Electrosorption-Enhanced Solid-Phase Microextraction Device for Ultrafast In Vivo Sampling of Ionized Pharmaceuticals in Fish, *Environ. Sci. Technol.*, 2018, **52**, 145–151.

7 Y.-H. Shih, C.-H. Chien, B. Singco, C.-L. Hsu, C.-H. Lin and H.-Y. Huang, Metal–organic frameworks: new matrices for surface-assisted laser desorption-ionization mass spectrometry, *Chem. Commun.*, 2013, **49**, 4929–4931.

8 L. Chen, J. Ou, H. Wang, Z. Liu, M. Ye and H. Zou, Tailor-Made Stable Zr(IV)-Based Metal–Organic Frameworks for Laser Desorption/Ionization Mass Spectrometry Analysis of Small Molecules and Simultaneous Enrichment of Phosphopeptides, *ACS Appl. Mater. Interfaces*, 2016, **8**, 20292–20300.

9 W. Ma, S. Xu, W. Ai, C. Lin, Y. Bai and H. Liu, A flexible and multifunctional metal–organic framework as a matrix for analysis of small molecules using laser desorption/ionization mass spectrometry, *Chem. Commun.*, 2019, **55**, 6898–6901.

10 Y. Zhang, B. E. G. Lucier, S. M. McKenzie, M. Arhangelskis, A. J. Morris, T. Friscic, J. W. Reid, V. V. Terskikh, M. Chen and Y. Huang, Welcoming Gallium- and Indium-Fumarate MOFs to the Family: Synthesis, Comprehensive Characterization, Observation of Porous Hydrophobicity, and CO_2 Dynamics, *ACS Appl. Mater. Interfaces*, 2018, **10**, 28582–28596.

11 M. J. Kalmutzki, C. S. Diercks and O. M. Yaghi, Metal–Organic Frameworks for Water Harvesting from Air, *Adv. Mater.*, 2018, **30**, 1704304.

12 K. Nath, A. Ahmed, D. J. Siegel and A. J. Matzger, Microscale Determination of Binary Gas Adsorption Isotherms in MOFs, *J. Am. Chem. Soc.*, 2022, **144**, 20939–20946.

13 N. C. Burtch, H. Jasuja and K. S. Walton, Water Stability and Adsorption in Metal–Organic Frameworks, *Chem. Rev.*, 2014, **114**, 10575–10612.

14 K. Joyaramulu, F. Geyer, A. Schneemann, S. Kment, M. Otyepka, R. Zboril, D. Vollmer and R. A. Fischer, Hydrophobic Metal–Organic Frameworks, *Adv. Mater.*, 2019, **31**, 1900820.

15 S. Yuan, L. Feng, K. Wang, J. Pang, M. Bosch, C. Lollar, Y. Sun, J. Qin, X. Yang, P. Zhang, Q. Wang, L. Zou, Y. Zhang, L. Zhang, Y. Fang, J. Li and H.-C. Zhou, Stable Metal–Organic Frameworks: Design, Synthesis, and Applications, *Adv. Mater.*, 2018, **30**, e1704303.

16 C. Wang, X. Liu, N. K. Demir, J. P. Chen and K. Li, Applications of water stable metal–organic frameworks, *Chem. Soc. Rev.*, 2016, **45**, 5107–5134.

17 J. J. Low, A. I. Benin, P. Jakubczak, J. F. Abrahamian, S. A. Faheem and R. R. Willis, Virtual High Throughput Screening Confirmed Experimentally: Porous Coordination Polymer Hydration, *J. Am. Chem. Soc.*, 2009, **131**, 15834–15842.

18 M. Ding, X. Cai and H.-L. Jiang, Improving MOF stability: approaches and applications, *Chem. Sci.*, 2019, **10**, 10209–10230.

19 S. Galli, A. Maspero, C. Giacobbe, G. Palmisano, L. Nardo, A. Comotti, I. Bassanetti, P. Sozzani and N. Masciocchi, When long bis(pyrazolates) meet late transition metals: structure, stability and adsorption of metal–organic frameworks featuring large parallel channels, *J. Mater. Chem. A*, 2014, **2**, 12208–12221.

20 C.-Y. Gao, J. Ai, H.-R. Tian, D. Wu and Z.-M. Sun, An ultrastable zirconium-phosphonate framework as bifunctional catalyst for highly active CO_2 chemical transformation, *Chem. Commun.*, 2017, **53**, 1293–1296.

21 J. Bedia, V. Muelas-Ramos, M. Penas-Garzon, A. Gomez-Aviles, J. J. Rodriguez and C. Belver, A Review on the Synthesis and Characterization of Metal Organic Frameworks for Photocatalytic Water Purification, *Catalysts*, 2019, **9**, 52.

22 X. Gong, K. Gnanasekaran, Z. Chen, L. Robison, M. C. Wasson, K. C. Bentz, S. M. Cohen, O. K. Farha and N. C. Gianneschi, Insights into the Structure and Dynamics of Metal–Organic Frameworks via Transmission Electron Microscopy, *J. Am. Chem. Soc.*, 2020, **142**, 17224–17235.

23 A. J. Howarth, A. W. Peters, N. A. Vermeulen, T. C. Wang, J. T. Hupp and O. K. Farha, Best Practices for the Synthesis, Activation, and Characterization of Metal–Organic Frameworks, *Chem. Mater.*, 2017, **29**, 26–39.

24 S. Bordiga, F. Bonino, K. P. Lillerud and C. Lamberti, X-ray absorption spectroscopies: useful tools to understand metallorganic frameworks structure and reactivity, *Chem. Soc. Rev.*, 2010, **39**, 4885–4927.

25 R. M. Stolz, A. Mahdavi-Shakib, B. G. Frederick and K. A. Mirica, Host-Guest Interactions and Redox Activity in Layered Conductive Metal–Organic Frameworks, *Chem. Mater.*, 2020, **32**, 7639–7652.

26 K. I. Hadjiivanov, D. A. Panayotov, M. Y. Mihaylov, E. Z. Ivanova, K. K. Chakarova, S. M. Andonova and N. L. Drenchev, Power of Infrared and Raman Spectroscopies to Characterize Metal–Organic Frameworks and Investigate Their Interaction with Guest Molecules, *Chem. Rev.*, 2021, **121**, 1286–1424.

27 X. Huang, H. Liu, D. Lu, Y. Lin, J. Liu, Q. Liu, Z. Nie and G. Jiang, Mass spectrometry for multi-dimensional characterization of natural and synthetic materials at the nanoscale, *Chem. Soc. Rev.*, 2021, **50**, 5243–5280.

28 Z. Lu, S. Deng, X. Liu, L. Huang, R. Zhang, H. Song and G. Li, Morphology and composition of particles emitted from conventional and alternative fuel vehicles, *Environ. Sci. Pollut. Res.*, 2021, **28**, 19810–19821.

29 C.-K. Chiang, W.-T. Chen and H.-T. Chang, Nanoparticle-based mass spectrometry for the analysis of biomolecules, *Chem. Soc. Rev.*, 2011, **40**, 1269–1281.

30 Y. Lin, X. Huang, Q. Liu, Z. Lin and G. Jiang, Thermal fragmentation enhanced identification and quantification of polystyrene micro/nanoplastics in complex media, *Talanta*, 2020, **208**, 120478.

31 L. Liu, B. He, Q. Liu, Z. Yun, X. Yan, Y. Long and G. Jiang, Identification and Accurate Size Characterization of Nanoparticles in Complex Media, *Angew. Chem., Int. Ed.*, 2014, **53**, 14476–14479.

32 Y. Jiang, J. Sun, C. Xiong, H. Liu, Y. Li, X. Wang and Z. Nie, Mass Spectrometry Imaging Reveals In Situ Behaviors of Multiple Components in Aerosol Particles, *Angew. Chem., Int. Ed.*, 2021, **60**, 23225–23231.

33 J. L. C. Rowsell and O. M. Yaghi, Effects of functionalization, catenation, and variation of the metal oxide and organic linking units on the low-pressure hydrogen adsorption properties of metal–organic frameworks, *J. Am. Chem. Soc.*, 2006, **128**, 1304–1315.

34 U. Mueller, M. Schubert, F. Teich, H. Puetter, K. Schierle-Arndt and J. Pastre, Metal–organic frameworks – prospective industrial applications, *J. Mater. Chem.*, 2006, **16**, 626–636.

35 S. Xu, S. Chansai, C. Stere, B. Inceesungvorn, A. Goguet, K. Wangkawong, S. F. R. Taylor, N. Al-Janabi, C. Hardacre, P. A. Martin and X. Fan, Sustaining metal–organic frameworks for water-gas shift catalysis by non-thermal plasma, *Nat. Catal.*, 2019, **2**, 142–148.

36 N. Al-Janabi, P. Hill, L. Torrente-Murciano, A. Garforth, P. Gorgojo, F. Siperstein and X. Fan, Mapping the Cu-BTC

metal–organic framework (HKUST-1) stability envelope in the presence of water vapour for CO_2 adsorption from flue gases, *Chem. Eng. J.*, 2015, **281**, 669–677.

37 Y. Lin, X. Huang, Y. Liu, D. Cao, D. Lu, Z. Feng, Q. Liu, Z. Lin and G. Jiang, Identification, Quantification, and Imaging of the Biodistribution of Soot Particles by Mass Spectral Fingerprinting, *Anal. Chem.*, 2021, **93**, 6665–6672.

38 J. Zou, H. Dong, H. Wu, J. Huang, X. Zeng, Y. Dou, Y. Yao and Z. Li, Laser-induced rapid construction of Co/N-doped honeycomb-like carbon networks as oxygen electrocatalyst used in zinc-air batteries, *Carbon*, 2022, **200**, 462–471.

39 L. R. Mingabudinova, A. S. Zalogina, A. A. Krasilin, M. I. Petrova, P. Trofimov, Y. A. Mezenov, E. V. Ubyivovk, P. Loennecke, A. Nomine, J. Ghanbaja, T. Belmonte and V. A. Milichko, Laser printing of optically resonant hollow crystalline carbon nanostructures from 1D and 2D metal–organic frameworks, *Nanoscale*, 2019, **11**, 13161.

40 Y.-H. Shih, C.-P. Fu, W.-L. Liu, C.-H. Lin, H.-Y. Huang and S. Ma, Nanoporous Carbons Derived from Metal–Organic Frameworks as Novel Matrices for Surface-Assisted Laser Desorption/Ionization Mass Spectrometry, *Small*, 2016, **12**, 2057–2066.

41 A. M. Ribeiro, T. P. Sauer, C. A. Grande, R. F. P. M. Moreira, J. M. Loureiro and A. E. Rodrigues, Adsorption equilibrium and kinetics of water vapor on different adsorbents, *Ind. Eng. Chem. Res.*, 2008, **47**, 7019–7026.

42 P. Li, J. Chen, J. Zhang and X. Wang, Water Stability and Competition Effects Toward CO_2 Adsorption on Metal Organic Frameworks, *Sep. Purif. Rev.*, 2015, **44**, 19–27.

43 J. B. DeCoste, G. W. Peterson, B. J. Schindler, K. L. Killops, M. A. Browe and J. J. Mahle, The effect of water adsorption on the structure of the carboxylate containing metal–organic frameworks Cu-BTC, Mg-MOF-74, and UiO-66, *J. Mater. Chem. A*, 2013, **1**, 11922–11932.

44 X. Sun, H. Li, Y. Li, F. Xu, J. Xiao, Q. Xia, Y. Lia and Z. Li, A novel mechanochemical method for reconstructing the moisture-degraded HKUST-1, *Chem. Commun.*, 2015, **51**, 10835–10838.

45 G. Majano, O. Martin, M. Hammes, S. Smeets, C. Baerlocher and J. Perez-Ramirez, Solvent-Mediated Reconstruction of the Metal–Organic Framework HKUST-1 (Cu-3(BTC)(2)), *Adv. Funct. Mater.*, 2014, **24**, 3855–3865.

46 S. Calero and P. Gomez-Alvarez, Insights into the Adsorption of Water and Small Alcohols on the Open-Metal Sites of Cu-BTC via Molecular Simulation, *J. Phys. Chem. C*, 2015, **119**, 467–472.

47 F. Gul-E-Noor, B. Jee, A. Poeppl, M. Hartmann, D. Himsl and M. Bertmer, Effects of varying water adsorption on a Cu-3(BTC)(2) metal–organic framework (MOF) as studied by H-1 and C-13 solid-state NMR spectroscopy, *Phys. Chem. Chem. Phys.*, 2011, **13**, 7783–7788.

48 O. Shekhah, J. Liu, R. A. Fischer and C. Woell, MOF thin films: existing and future applications, *Chem. Soc. Rev.*, 2011, **40**, 1081–1106.

49 W.-J. Li, M. Tu, R. Cao and R. A. Fischer, Metal–organic framework thin films: electrochemical fabrication techniques and corresponding applications & perspectives, *J. Mater. Chem. A*, 2016, **4**, 12356–12369.

50 N. Al-Janabi, A. Alfutimie, F. R. Siperstein and X. Fan, Underlying mechanism of the hydrothermal instability of Cu-3(BTC)(2) metal–organic framework, *Front. Chem. Sci. Eng.*, 2016, **10**, 103–107.

51 S. Shang, Z. Tao, C. Yang, A. Hanif, L. Li, D. C. W. Tsang, Q. Gu and J. Shang, Facile synthesis of CuBTC and its graphene oxide composites as efficient adsorbents for CO_2 capture, *Chem. Eng. J.*, 2020, **393**, 124666.